ORIGINAL PAPER

In situ X-ray absorption spectroscopy of Sn species adsorbed on platinized platinum electrode in perchloric acid solution containing stannous ions

M. Seo[1] · H. Habazaki[1] · M. Inaba[2] · M. Yokomizo[3] · T. Nakayama[4]

Abstract

In situ X-ray absorption spectroscopy (XAS) was applied to investigate the Sn adlayer on platinized (pl-) Pt electrode in deaerated 0.2 M HClO$_4$ solution containing 10^{-3} M Sn^{2+} in relation to the effect of Sn addition on electrocatalysis of Pt. A periodical emersion method under potentiostatic polarization, using pl-Pt plate (roughness factor S_r = 770) as a working electrode was employed to detect sensitively the sub-monolayer coverage of Sn on Pt. The Sn K-edge absorption spectra in a scanning XAS mode were measured by monitoring the Sn K$_{\alpha 1}$ fluorescence line. The Sn K-edge absorption near-edge structure (XANES) has indicated that the Sn species adsorbed on the pl-Pt electrode is partly oxygenated in the Sn-underpotential (UPD) region between − 0.05 and 0.25 V (RHE) which is overlapped with the UPD region of hydrogen. The extended X-ray absorption fine structure (EXAFS) analysis has supported a Sn overlayer model in which Sn atom occupies the hollow site of the nearest neighbor Pt atoms and is further bound with oxygen atoms in the Sn-UPD region. The coordination number of the Sn–Pt bond or Sn–Sn bond decreases with increasing potential, while the coordination number of the Sn–O bond increases reversely. In the potential region between 0.45 and 0.85 V (RHE), the EXAFS analysis has suggested that two-dimensional surface Sn oxide forms on the pl-Pt electrode, which is supported from the potential-pH equilibrium diagram of the Sn/H$_2$O system.

Keywords In situ XAS · EXAFS · Underpotential deposition (UPD) of Sn · Sn adsorption structure · Platinized Pt

Introduction

It has been reported that the addition of Sn to Pt enhances the electrocatalytic reaction of Pt such as electro-oxidation of CO [1–4], HCOOH [4–6], or methanol [3, 6–9], which is promising as anodic materials for low-temperature fuel cells. In contrast, the negative or poor effect of Sn addition on the electrocatalytic reaction of Pt has been also reported, e.g., for methanol oxidation [10–12]. A variety of methods are used to add Sn to Pt: (1) underpotential deposition (UPD) of Sn on Pt [1, 5, 6, 8, 13], (2) alloy formation as a bimetallic electrocatalyst [2, 14–18], and (3) co-deposition of Pt and of Sn/SnO$_x$ [19–23]. As reviewed by Antolini and Gonzalez [3], the electrocatalytic activity of Pt depends on the chemical states, local structures, composition, or coverage of Sn species (adatom, alloyed, or oxygenated). X-ray absorption spectroscopy (XAS) [24–26], using a synchrotron radiation, is a powerful tool for investigating the chemical state and local structure of dispersed species as adatoms or alloying elements in electrocatalysts. The X-ray absorption near-edge structure (XANES) within about 50 eV above the absorption edge provides the information of the chemical state and electronic structure of the absorbing atom, while the extended X-ray absorption fine structure (EXAFS) up to 1000 eV provides information of local structure of the nearest neighbor atoms such as inter-atomic distance and coordination number. XAS, therefore, has been increasingly applied to the study of fuel cell catalysts, particularly containing Pt for use in low temperature [27].

✉ M. Seo
    masaseo@eng.hokudai.ac.jp

[1] Division of Applied Chemistry, Faculty of Engineering, Hokkaido University, Sapporo, Hokkaido 060-8628, Japan

[2] Kobelco Research Institute, Inc., Fujisawa Section, Fujisawa, Kanagawa 251-0014, Japan

[3] Kobelco Research Institute, Inc., Seishin Section, Kobe, Hyogo 651-2271, Japan

[4] Materials Research Laboratory, Kobe Steel Ltd., Kobe, Hyogo 651-2271, Japan

The effects of Sn added with different methods to carbon- or silica-supported Pt electrocatalysts have been also investigated by in situ XAS [28–35]. The studies [4, 8, 13] of electrocatalytic activity of Pt modified by Sn-UPD were mostly performed in acid solutions free from Sn ions after Sn species was adsorbed on Pt in perchloric acid or sulfuric acid containing $SnCl_4$, $Sn(SO_4)_2$ or $Sn(ClO_4)_4$. However, the chemical state and local structure of the Sn species on Pt in acid solution free from Sn ions after the Sn adsorption may be different from those of the Sn species adsorbed on Pt under potential control in acidic solution containing Sn ions, since the Sn species on Pt in acid solution free from Sn ions is not in equilibrium with Sn ions in acidic solution. There have been no in situ XAS studies of Sn species adsorbed on Pt under potential control in acid solution containing Sn ions. Therefore, it is essentially important from the fundamental viewpoint to evaluate the chemical state and local structure of the Sn species adsorbed on Pt under potential control in acid solution containing Sn ions. However, the in situ XAS measurement of the Sn species adsorbed on Pt in acid solution containing Sn ions raises difficulties in the way of avoiding the contribution of Sn ions in acid solution to Sn-XAS spectra.

The emersion method developed by Hansen et al. [36, 37] for spectroscopy of the solid electrode/solution interface may be useful to avoid the contribution of metal ions in solution. Moreover, Stefan and Scherson [38] developed the rotated emersion method for the study on passivity of Zn in an alkaline solution and succeeded in monitoring the growth and reduction processes of passive film. A grazing incidence-excitation technique for the in situ XAS measurements of UPD layers [39–45] on noble metal electrodes has been employed to detect sensitively the sub-monolayer. The grazing incidence-excitation technique, however, is not always necessary in the case where the specimen with large surface roughness is prepared. We have recently developed a periodical emersion method [46, 47] using a surface-roughened Ni (sr-Ni) plate for in situ XAS study of the Pb- or Sn-UPD layer on Ni in acidic perchlorate solution containing Pb^{2+} or Sn^{2+} and succeeded in evaluating the chemical state and local structure of the respective UPD layer as a function of applied potential from the measurements of the Pb L_3-edge or Sn K-edge XAS spectra, which leads to the more comprehensive understanding of the inhibition effect of Pb or Sn on corrosion of Ni.

In this study, the periodical emersion method [46, 47] was employed to measure the Sn K-edge XAS spectra of the Sn species adsorbed on Pt in perchloric acid containing Sn^{2+} as function of applied potential. For this purpose, a platinized platinum (pl-Pt) was electro-deposited on Pt plate to enlarge the surface roughness. In preparation of Pt electrocatalysts, nano-Pt particles are usually supported with carbon or silica. However, the adsorption on supporter such as carbon [30] has to be taken into consideration for the study of adsorption on supported Pt electrocatalysts. The choice of the pl-Pt plate in this study provides an additional advantage of avoiding the complications of Sn adsorption on supporter. The EXAFS analysis of Sn K-edge spectra for the Sn species adsorbed on pl-Pt electrode in perchloric acid containing Sn^{2+} has provided a new result that proves the presence of the Sn–Pt or Sn–Sn bond in addition to the Sn–O bond in the potential range between − 0.05 and 0.25 V (RHE), which is not consistent with the previous EXAFS results [31] of the Sn species on Pt in acid solution free from Sn ions after the Sn adsorption. The difference in Sn species on Pt will be discussed from the comparison between the present and previous results.

Experimental

Preparation of specimen and electrolyte

Polycrystalline Pt plate with a size of $20 \times 25 \times 0.2$ mm (purity > 99.99%, Tanaka Kikinzoku kogyo, Co., Ltd.) was used as a substrate. It was rinsed in concentrated H_2SO_4 and then washed with ultrapure water supplied through a super Milli-Q filter system. Two pieces of Pt plates were alternatively anodically and cathodically polarized 11 times for each 30 s at a constant current density of 60 mA cm^{-2} in 6.3×10^{-2} M hydrogen hexachloroplatinate (IV) hexahydrate, $H_2PtCl_6 \cdot 6H_2O$, containing 1.03×10^{-3} M lead acetate, $Pb(CH_3COO)_2$, to obtain platinized platinum (pl-Pt) deposit. The above preparation condition of the pl-Pt deposit is in accordance with the condition in the literature [48] for obtaining a maximum surface roughness. Subsequently, the Pt plates with pl-Pt deposit were alternatively anodically and cathodically polarized 20 times for each 60 s at a constant current density of 6 mA cm^{-2} in 1 M H_2SO_4 to remove the Pb species from the pl-Pt deposit and stored in a glass bottle filled with ultrapure water. Prior to experiments, the surface and cross-section morphologies of the pl-Pt deposit were observed with a SEM (JSM-6500F, JEOL). Moreover, the atomic structure of the pl-Pt deposit was examined with a Cs-corrected TEM (Titan 3 G2 60-300, FEI Co.). For TEM imaging, the pl-Pt particles collected by mechanically scraping the pl-Pt plate with a spatula were dispersed in ethanol with an aid of ultrasound. Afterwards, a drop of the suspension was deposited onto a holey carbon film supported by a Cu grid. The TEM images were measured at an accelerating voltage of 300 kV.

The electrolyte solution used for experiments was 0.2 M $HClO_4$ solution containing 10^{-3} M Sn^{2+}. Tin was added as SnO to give 10^{-3} M Sn^{2+} in solution. The choice of SnO as Sn^{2+} source in place of $SnCl_2$ or $SnSO_4$ was made to avoid the influence of electrolyte anions such as Cl^- or SO_4^{2-} on Sn adsorption. The electrolyte solution was prepared from guaranteed grade 60% $HClO_4$ (Kanto Chemical Co. Inc.) and high purity (> 99.5%) SnO (Koujundo Chemical Lab. Co. Ltd.)

with ultrapure water supplied through a super Milli-Q filter system. During preparation of the solution containing 10^{-3} M Sn^{2+}, the possibility for an oxidation of Sn^{2+} to Sn^{4+} by air dissolved in solution is not excluded [47, 49]. The Sn^{4+} species in solution, however, should be minor since the solution is deaerated in a reservoir immediately after the preparation.

In situ XAS measurement

The XAS measurements were performed at the BL16B2 beam line of SPring-8, Hyogo, Japan. The electrochemical cell was so mounted on a stage as to locate the Kapton window side at an angle of 45° relative to the incident X-ray beam. The pl-Pt electrode was set into the cell in parallel to the Kapton window. The distance between pl-Pt electrode and Kapton window was kept about 1 mm. After air in the cell was completely removed by flowing ultrapure argon gas in the cell, the electrolyte solution was supplied from the solution reservoir up to the level H in the cell at which the pl-Pt electrode was fully immersed in solution. The potential of the pl-Pt electrode was measured with an Ag/AgCl/sat. KCl reference electrode through a Luggin capillary tube and referred to the reversible hydrogen electrode (RHE) in 0.2 M $HClO_4$. A Pt plate was used as a counter electrode.

At first, the pl-Pt electrode was potentiostatically polarized in the solution until the polarization current attained steady state. It took about 30 min to attain almost the steady state. Afterwards, the periodical emersion of the pl-Pt electrode under potentiostatic polarization was made as follows: (1) the solution in the cell was lowered to the level L at which the upper part of the pl-Pt electrode was emerged and the X-ray beam was irradiated to the part of the pl-Pt electrode emerged from the level L for data collection by a scanning XAS mode; (2) after the data collection for 2 min, the solution was raised to the level H and the pl-Pt electrode was fully immersed in the solution for 2 min; and (3) the solution was lowered again to the level L for data collection and the above procedure was repeated at least ten cycles. The level H was higher by 10 mm than the level L. The volumes of the solution in the cell at levels H and L were 273 and 228 cm^3, respectively. The X-ray beam was irradiated to the rectangular area (2 mm × 7 mm) of the pl-Pt electrode located at the middle of the levels H and L, i.e., above 5.0 mm from the level L. Details of the electrochemical cell and solution level-control system for the periodical emersion method were described elsewhere [46, 47].

The Sn K-edge absorption spectra were measured by monitoring the Sn $K_{\alpha 1}$ fluorescence line at 25.27 keV obtained from a 19-element Germanium Array Detector (Canberra, Inc.). The incident X-ray beam was collimated with slits to the rectangle of 5 mm in length × 2 mm in width. The Si (111) double-crystal monochromator was used and the photon energy was calibrated relative to the sharp pre-edge peak (8.9803 keV) of metallic Cu. The photon energy was scanned from

28.90 to 30.70 keV for 2 min to collect the fluorescence data. Afterwards, the photon energy was scanned back to 28.90 keV for 1 min. The scanning time of the photon energy was synchronized with the periodical emersion through the combination of DAQ (NI PCI-MIO-16XE-50) for the XAS measurement and LabVIEW software for the solution-control system. The Sn K-edge absorption spectra of metallic β-Sn foil and SnO_2 (cassiterite) as standard materials were also measured in the same photon energy range for comparison.

Results and discussion

Surface morphology and atomic structure of the pl-Pt deposit

Figure 1a shows the cross-section of the SEM image of the pl-Pt deposit. It is seen from Fig. 1a that the average thickness of the deposit is about 10 μm. The SEM image at a high
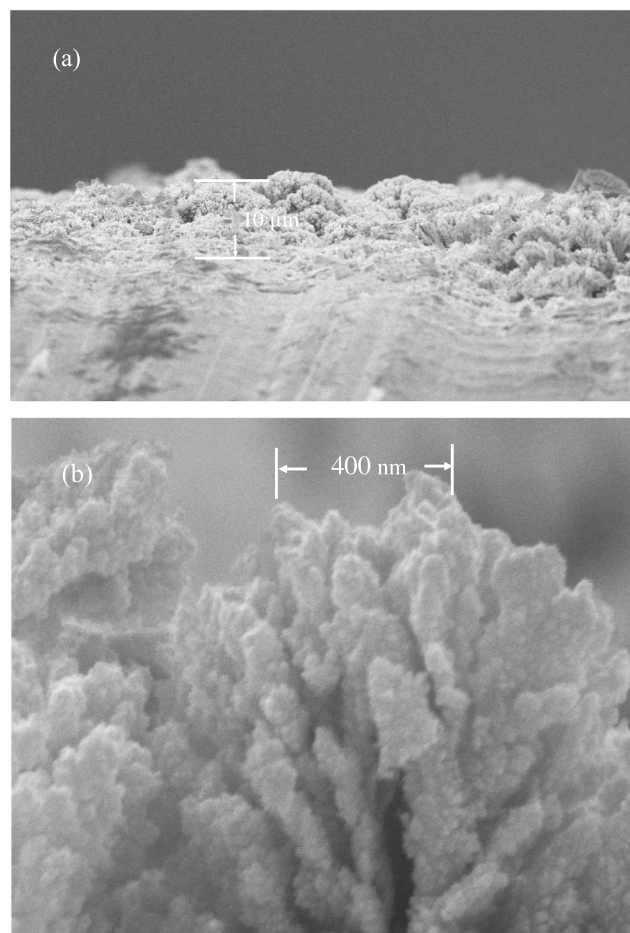
Fig. 1 **a** SEM image of the cross-section of the platinized (pl-) Pt deposit. The average thickness of the deposit is about 10 μm. **b** SEM image of the pl-Pt deposit at a high magnification (× 50000). The deposit layer consists of an aggregation of leafy structures

magnification (× 50000) in Fig. 1b indicates that the deposit layer consists of an aggregation of leafy structures. Figure 2a shows the TEM image of the separated leafy structure. Furthermore, the edge part of the leaf structure is magnified in Fig. 2b, revealing the presence of the palm- and finger-like shapes in the nanometer size. Figure 2c shows the atomic-resolution TEM image of the finger-like shapes. The minimum diameter at the round tip of finger is about 3 nm. The lattice information of the pl-Pt deposit such as spacing d_{hkl} of lattice plane $(h\,k\,l)$ and lattice constant, $a_0 = d_{hkl}\sqrt{h^2 + k^2 + l^2}$, can be determined from the periodical atomic arrays in Fig. 2c. The values of $d_{200} = 2.07 \sim 2.08$ Å for the Pt (200) plane were obtained as marked in Fig. 2c.

The atomic-resolution TEM images were also measured at many different positions (not only for the edge but also for the inside part) of the leafy structure. The values of d_{200} ranged from 2.04 to 2.08 Å depending on the measured positions. In addition, the values of $d_{111} = 2.30 \sim 2.35$ Å for the Pt (111) plane were also observed. However, the majority area was oriented to the (200) plane as compared to the (111) plane. The values of a_o calculated from the average values of d_{200} and d_{111} were 4.12 and 4.03 Å, respectively, that were larger by 5.0 and 2.7 % than that ($a_0 = 3.923$ Å) of bulk Pt. Du et al. [50], using high-resolution TEM, have found that the lattice parameter of Pt nanoparticles is expanded by 1.3~4.8% than that of bulk Pt, insensitive of the particle size in the observed regime (2.5~5.0 nm) of particle diameters. The lattice parameter expansion was ascribed to an amorphous oxide on the nanoparticles surface and/or dissolution of oxygen in sub-surface sites [50].

Polarization behavior of the pl-Pt electrode

Figure 3a shows the cyclic voltammogram (CV) of the pl-Pt electrode measured at a potential sweep rate of 10 mV s^{-1} in the narrow potential range between − 0.02 and 0.52 V (RHE) in deaerated 0.2 M HClO$_4$ solution. A regular electrochemical cell made from glassware was used for the CV measurement. The current density, i, in the ordinate of Fig. 3a was obtained with dividing the current by the geometrical surface area of the pl-Pt electrode. The doublet cathodic current peaks observed at 0.34 V and 0.13 V (RHE) result from the underpotential deposition (UPD) of hydrogen ions (H$^+$) on Pt, while the doublet anodic current peaks at 0.15 V and 0.35 V (RHE) are caused by the anodic stripping of the underpotential-deposited hydrogen atoms on Pt. The cathodic charge, Q_c, and anodic charge, Q_a, in the potential region between 0.0 and 0.42 V (RHE) in 0.2 M HClO$_4$ were 0.169 C cm^{-2} and 0.155 C cm^{-2}, respectively. The electric double-layer charges in cathodic and anodic potential sweeps were subtracted from the total cathodic and anodic charges to
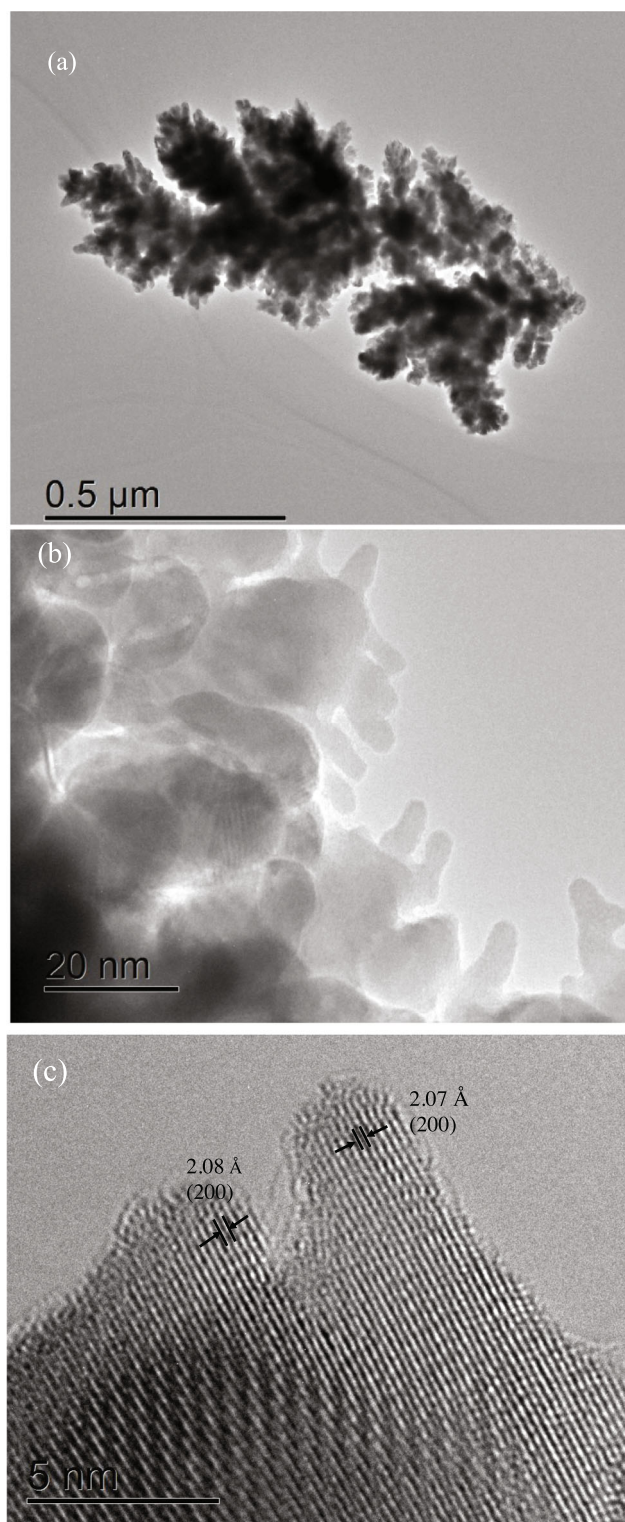
Fig. 2 a TEM image of the separated leafy structure in the pl-Pt deposit. **b** Magnified TEM image of the edge part of the leaf structure. The palm- and finger-like shapes in nanometer size are observed. **c** Atomic-resolution TEM image of the finger-like shapes. The lattice information of the pl-Pt such as spacing d_{hkl} of lattice plane $(h\,k\,l)$ and lattice constant, $a_0 = d_{hkl}\sqrt{h^2 + k^2 + l^2}$, can be determined from the periodical atomic arrays in **c**. The values of $d_{200} = 2.07$ or 2.08 Å for the (200) plane were obtained as marked in **c**
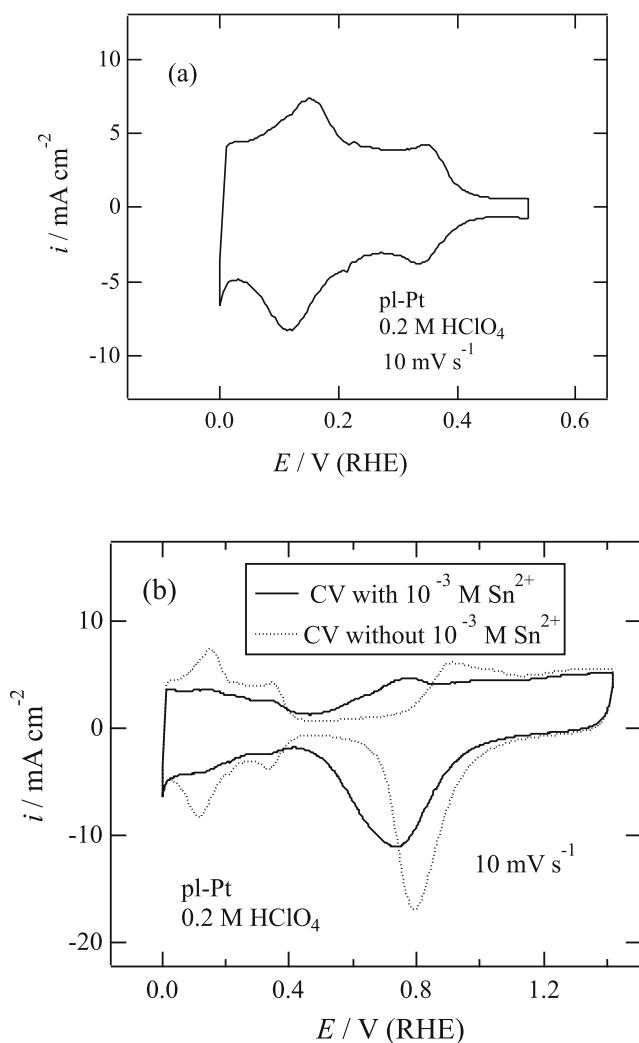
Fig. 3 **a** Cyclic voltammogram (CV) of the pl-Pt electrode measured at a potential sweep rate of 10 mV s^{-1} in the narrow potential range between − 0.02 and 0.52 V (RHE) in deaerated 0.2 M HClO$_4$ solution. The current density, i, in the ordinate of **a** was obtained with dividing the current by the geometrical surface area of the pl-Pt electrode. **b** Cyclic voltammograms (CVs) of the pl-Pt electrode measured at a potential sweep rate of 10 mV s^{-1} in the wide potential range between − 0.02 and 1.42 V (RHE) in deaerated 0.2 M HClO$_4$ solutions with (solid curve) and without 10^{-3} M Sn^{2+} (dotted curve). The addition of 10^{-3} M Sn^{2+} reduces significantly the doublet cathodic and anodic current peaks in the potential region between 0.0 and 0.42 V (RHE)

determine Q_c and Q_a. The average value of Q_c and Q_a, i.e., $Q_{av} = 0.162$ C cm^{-2} corresponds to the electric charge required for the formation of hydrogen monolayer (H:Pt = 1:1) on pl-Pt electrode. According to the literatures [48, 51–55], the electric charge for the formation of hydrogen monolayer on a flat polycrystalline Pt is 210 μC cm^{-2}, from which the surface roughness factor, S_r, of the pl-Pt electrode is estimated to be 770. Figure 3b shows the cyclic voltammograms (CVs) of the pl-Pt electrode measured at a potential sweep rate of 10 mV s^{-1} in the wide potential range between − 0.02 and 1.42 V (RHE) in deaerated 0.2 M HClO$_4$ solutions with and without 10^{-3} M Sn^{2+}.
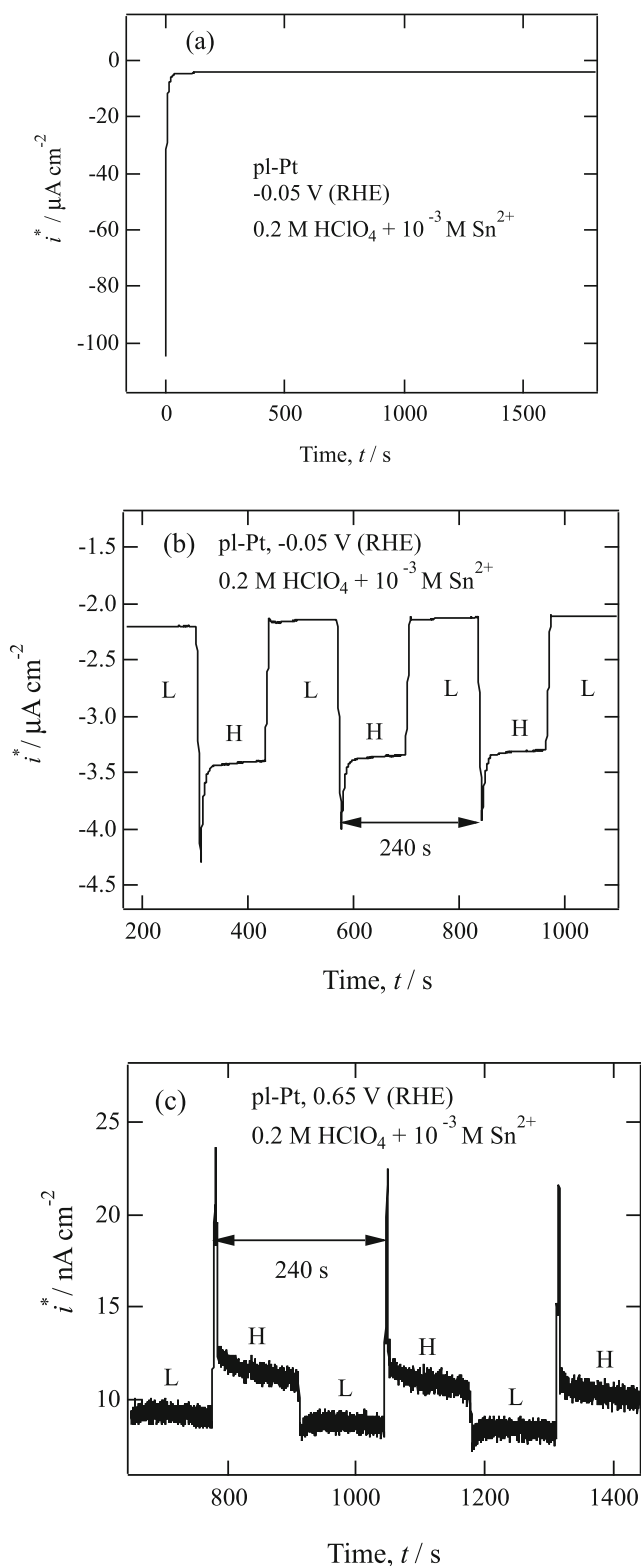
The addition of 10^{-3} M Sn^{2+} reduces significantly the doublet cathodic and anodic current peaks in the potential region between 0.0 and 0.42 V (RHE).

According to Kolb et al. [56, 57], the potential window in which UPD proceeds, ΔE_{UPD}, can be approximately estimated from the following empirical relation:

$$\Delta E_{UPD} \approx 0.5 \frac{(\Phi_S - \Phi_M)}{e}, \qquad (1)$$

where Φ_S and Φ_M are the work functions of foreign substrate and UPD metals, respectively, and e is the elementary charge. If taking $\Phi_S = 5.65$ eV for polycrystalline Pt [33] and $\Phi_M = 4.42$ eV for polycrystalline Sn [58], $\Delta E_{UPD} \approx 0.615$ V is obtained from Eq. (1). Since the equilibrium potential of the (10^{-3} M Sn^{2+}/Sn) system is − 0.172 V (RHE) in 0.2 M HClO$_4$ [47], the Sn-UPD potential region estimated for the (10^{-3} M Sn^{2+}/Pt) system is from − 0.172 to 0.443 V (RHE), which is overlapped with the potential region of hydrogen-UPD between 0.0 and 0.42 V (RHE). Consequently, the reduction in the doublet cathodic and anodic current peaks in the hydrogen-UPD region due to the addition of Sn^{2+} may result from the competitive UPD of Sn and hydrogen on Pt. In the anodic potential sweep (Fig. 3b), the anodic current in the presence of Sn^{2+} increases at potentials higher than about 0.45 V (RHE) and an anodic peak appears at about 0.77 V (RHE), which is associated with anodic oxidation of the Sn species on Pt, while the anodic current in the absence of Sn^{2+} increases at potentials higher than about 0.75 V (RHE) and an anodic current peak appears at about 0.90 V (RHE), which corresponds to the formation of surface Pt oxide film. The decrease in anodic current without anodic peak at potentials higher than 0.85 V (RHE) in the presence of Sn^{2+} suggests that the oxidized Sn species on Pt inhibits the formation of surface Pt oxide film. In the cathodic potential sweep (Fig. 3b), the cathodic current peak in the presence of Sn^{2+} appears at about 0.75 V (RHE), while the cathodic current peak in the absence of Sn^{2+} appears at about 0.80 V (RHE). The broad cathodic current peak in the presence of Sn^{2+} as compared to the sharp cathodic current peak in the absence of Sn^{2+} may result from the overlapped cathodic reduction of oxidized Sn species on Pt and of surface Pt oxide film. The results of Fig. 3b are almost consistent with the previous reports [8, 13].

The pl-Pt electrode was potentiostatically polarized at seven different potentials of − 0.05 V, 0.05 V, 0.15 V, 0.25 V, 0.45 V, 0.65 V, and 0.85 V (RHE) in deaerated 0.2 M HClO$_4$ with 10^{-3} M Sn^{2+}. An incipient oxide film on Pt can be easily reduced at − 0.05 V (RHE). Therefore, the Sn K-edge XAS measurement was initiated at − 0.05 V (RHE) to avoid the influence of an incipient Pt oxide film on the XAS measurement and subsequently was made in turn at the more noble potential. Figure 4a shows the time–variation of current density during potentiostatic polarization of the pl-Pt electrode at

decreases rapidly at the initial stage, involving in hydrogen evolution in addition of Sn- and hydrogen-UPD on the pl-Pt electrode. The cathodic current density almost attains to a steady state after 30 min. The cathodic current density (less than − 4 μA cm^{-2}) after 30 min is mainly due to hydrogen evolution. The hydrogen bubbles on the pl-Pt electrode, however, could not be observed with the naked eye.

Figure 4b shows the changes in current density of the pl-Pt electrode at − 0.05 V (RHE) in the solution with 10^{-3} M Sn^{2+} during periodical emersion-XAS measurement. The current density changes periodically at − 0.05 V (RHE) synchronized with the periodical changes between solution levels H and L in the electrochemical cell. The marks, L and H, in Fig. 4b correspond to the solution levels L and H, respectively. The ratio (0.63) of L to H current plateau is almost consistent with the surface area ratio (0.6) of the pl-Pt electrode immersed in solution. The instantaneous overshoots of current density are observed during every transition from the solution level L to H, which may be caused by electric noises from the control system of solution level. When the potential of pl-Pt electrode fully immersed in solution was changed from − 0.05 to 0.05 V (RHE), a cathodic current flowed and the cathodic current density, i^*, in steady state at 0.05 V (RHE) was less than − 12 nA cm^{-2}. An anodic current flowed at the potential more positive than 0.15 V (RHE) and the anodic current density, i^*, in steady state was in the order of nanoamperes per square centimeter. Figure 4c shows the changes in current density of the pl-Pt electrode at 0.65 V (RHE) during periodical emersion-XAS measurement, indicating that the periodical changes of anodic current plateaus in solution levels L and H are in the order of nanoamperes per square centimeter. However, it should be remarked that the Sn adsorption behavior on the pl-Pt electrode under stepwise-potentiostatic polarization employed for the present XAS measurement is not always the same as that under the cyclic voltammetry (CV) shown in Fig. 3b, since the history of the pl-Pt electrode is different between stepwise polarization and CV.

− 0.05 V (RHE) in the solution with 10^{-3} M Sn^{2+}. The current density, i^*, in the ordinate in Fig. 4a was obtained with dividing the current by the real surface area (surface roughness, $S_r = 770$) of the pl-Pt electrode. The cathodic current density

Sn K-edge spectra

Figure 5 shows the raw Sn K-edge XAS spectrum (solid curve) collected by ten times energy scanning and averaged for the pl-Pt electrode kept at 0.25 V (RHE). The Sn $K_{\alpha 1}$ fluorescence intensity divided by the incident X-ray intensity was taken as absorbance, μt, in the ordinate of Fig. 5. The sharp rise of the spectrum in Fig. 5 corresponds to the Sn K-edge. As previously reported [47], the inevitable issue for Sn-XAS analysis is that some kinds of Sn species from Sn^{2+}-containing solution are adhered to the inside wall of the Kapton window. The Sn K-edge XAS spectrum of the Kapton window was measured under the same experimental conditions by removing the pl-Pt electrode from the electrochemical cell after every XAS measurement. The intensity level of Sn K-edge spectrum of the Kapton window was almost constant and independent of the number of XAS measurement, indicating that the amount of Sn species adhered to the Kapton window is saturated. The precipitation [49] of Sn colloid on the Kapton window may occur during deaeration of the Sn^{2+}-containing solution in electrochemical cell before the beginning of XAS measurement. The Sn K-edge spectrum (dotted curve) of the Kapton window is represented by "blank" in Fig. 5 for comparison. The intensity of the blank spectrum is about 20% of that of the spectrum measured for the pl-Pt electrode at 0.25 V (RHE). Nevertheless, an attempt to get the real spectra of Sn species on the pl-Pt electrode was made by subtracting the blank spectrum from the spectra measured for the pl-Pt electrode since the blank spectrum intensity
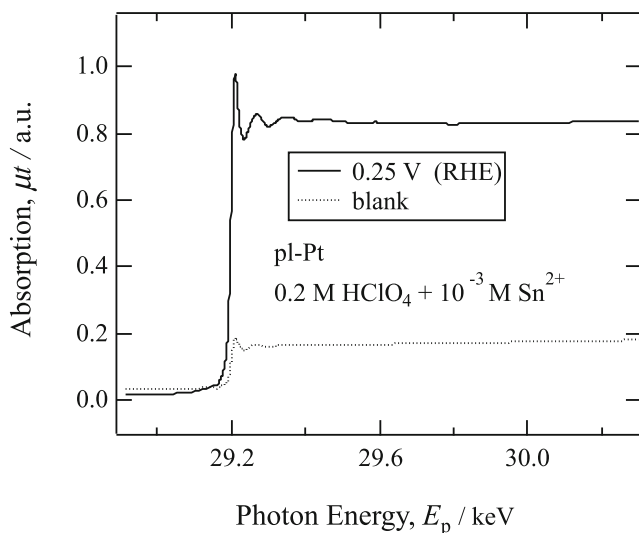
attained already to the steady state and did not change for every experiment.

Figure 6 shows the typical X-ray absorption near-edge structure (XANES) spectra of Sn K-edge for the pl-Pt electrode kept at three different potentials of -0.05 V, 0.25 V, and 0.65 V (RHE), normalized after the subtraction of the blank spectrum. The normalized Sn K-edge XANES spectra of metallic β-Sn foil and SnO_2 are also shown in Fig. 6 for comparison. The normalized Sn K-edge XANES spectrum for the pl-Pt electrode at -0.05 V (RHE) is close to that of metallic β-Sn foil. In addition, the normalized Sn K-edge XANES spectrum for the pl-Pt electrode shifts towards that of SnO_2 with increasing potential from -0.05 to 0.85 V (RHE), although the spectra measured at other four potentials of 0.05 V, 0.15 V, 0.45 V, and 0.85 V (RHE) are not shown in Fig. 6, suggesting that the chemical state of the Sn species on pl-Pt electrode changes to the more oxidative state with increasing potential. The potential dependence of the Sn species on pl-Pt electrode is discussed later from the extended X-ray absorption fine structure (EXAFS) analysis.

The trace amount of solution may remain on the pl-Pt electrode surface with a large roughness factor of $S_r = 770$ due to capillary action during emersion to give the contribution of Sn^{2+} ions to the measured Sn K-edge XAS spectra. The average thickness of the solution remained on the pl-Pt electrode surface was estimated to be about 30 μm per geometrical surface area of the pl-Pt electrode from the gravimetrical measurement. The amount of Sn^{2+} ions in the solution with a thickness of 30 μm is 1.8×10^{15} ions cm^{-2}. The amount of Sn species underpotential-deposited on Pt in the UPD potential range more noble than the equilibrium potential of Sn^{2+}/Sn
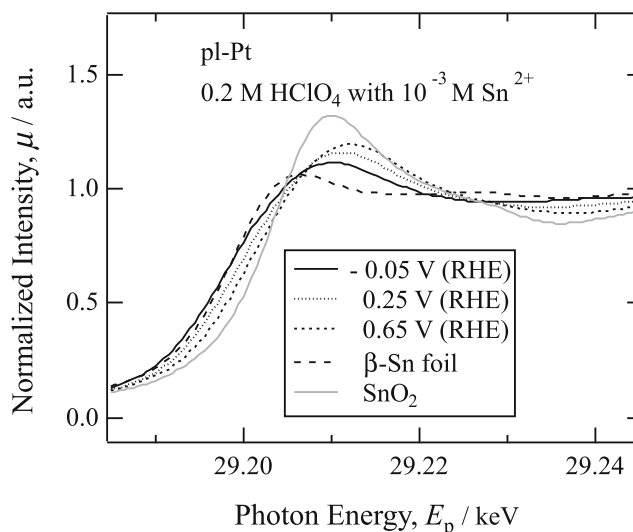

Fig. 5 Raw Sn K-edge XAS spectrum (solid curve) collected by ten times energy scanning and averaged for the pl-Pt electrode kept at 0.25 V (RHE). The Sn $K_{\alpha 1}$ fluorescence intensity divided by the incident X-ray intensity was taken as absorbance, μt, in the ordinate of Fig. 5. The Sn K-edge XAS spectrum (dotted curve) of the Sn species adhered to the inside wall of the Kapton window is represented by "blank" in Fig. 5 for comparison


Fig. 6 Typical X-ray absorption near-edge structure (XANES) spectra of Sn K-edge for the pl-Pt electrode kept at three different potentials of $-$ 0.05 V, 0.25 V, and 0.65 V (RHE), normalized after the subtraction of the blank spectrum. The normalized Sn K-edge XANES spectra of metallic β-Sn foil and SnO_2 are also shown in Fig. 6 for comparison

would not exceed the Sn monolayer as generally accepted for many UPD systems [57, 59]. The amount of Sn atoms corresponding to the monolayer on a flat polycrystalline Pt surface is calculated to be 1.3×10^{15} atoms cm^{-2} by taking the difference in atomic radius between Sn ($r_{Sn} = 1.405$ Å for α-Sn) and Pt ($r_{Pt} = 1.385$ Å) into account. Therefore, the amount of Sn atoms corresponding to the monolayer on the pl-Pt electrode surface is estimated to be 1.0×10^{18} atoms cm^{-2} by multiplying 1.3×10^{15} atoms cm^{-2} by the roughness factor ($S_r = 770$). The amount (1.8×10^{15} ions cm^{-2}) of Sn^{2+} ions in the solution layer remained on the pl-Pt electrode is only 0.2% of the Sn monolayer, suggesting that the contribution of Sn^{2+} ions to the measured Sn K-edge XAS spectra is negligibly small even if the surface coverage of Sn species on the pl-Pt electrode is less than the Sn monolayer. The emerged area of the pl-Pt electrode should be electrochemically controlled since the thin solution layer of about 30 μm remained on the emerged area due to capillary action is connected with the bulk solution.

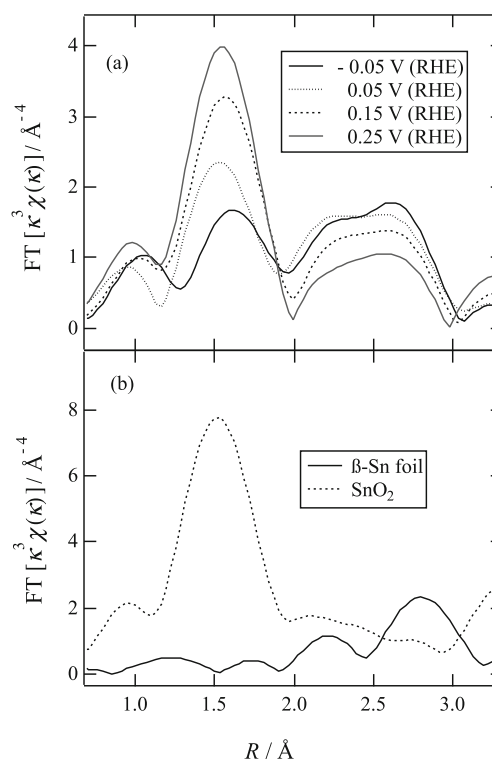## EXAFS analysis of Sn K-edge spectra

The local atomic structure of the Sn species on pl-Pt electrode and its potential dependence can be evaluated from the EXAFS analysis. The oscillatory part, $\chi(\kappa)$, of the Sn K-edge XAS spectrum above the absorption edge for the pl-Pt electrode was extracted as a function of wave number, κ, by removing the smooth background. Figure 7 shows the κ^3-weighted EXAFS functions ($\kappa^3\chi$ vs. κ curves) obtained from the Sn K-edge XAS spectra for the pl-Pt electrode kept at − 0.05 V, 0.25 V, and 0.65 V (RHE). The EXAFS features depending on potential are discernible from Fig. 7. Nevertheless, the EXAFS function data in the low potential region between
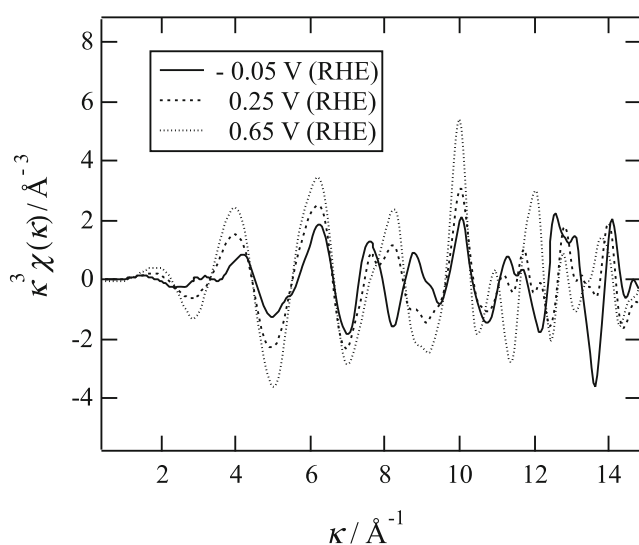
− 0.05 and 0.25 V (RHE) are noisy in the κ range higher than 11.0 Å^{-1}, although the data at other potentials are not shown in Fig. 7. The subtraction of the blank spectrum from the raw XAS spectra (Fig. 5) may lead to the noisy EXAFS data in the high κ-range. The windows of $\kappa = 2.0$ Å^{-1} to 11.0 Å^{-1} and of $\kappa = 2.0$ Å^{-1} to 12.5 Å^{-1} were set for Fourier transforming the EXAFS data in the low potential region between − 0.05 and 0.25 V (RHE) and in the high potential region between 0.45 and 0.85 V (RHE), respectively.

Figure 8a, b shows the radial structure functions, RSFs (FT[$\kappa^3\chi(k)$] vs. R curves) obtained by Fourier transforming the EXAFS data in the κ range of 2.0 Å^{-1} to 11.0 Å^{-1} for the pl-Pt electrode kept in the low potential region and for the Sn standard materials (β-Sn foil and SnO$_2$), respectively. The single peak at $R = 1.54~1.63$ Å in the RSFs of the pl-Pt electrode (Fig. 8a) corresponds to that at $R = 1.53$ Å in the RSF of SnO$_2$ (Fig. 8b). In addition, the doublet or broad peak at $R = 2.3~2.7$ Å in the RSFs of the pl-Pt electrode (Fig. 8a) is situated near the doublet peak at $R = 2.25~2.8$ Å in the RSF of metallic β-Sn foil (Fig. 8b). Figure 9a, b shows the radial structure functions, RSFs (FT[$\kappa^3\chi(k)$] vs. R curves) obtained by Fourier transforming the EXAFS data in the κ range of 2.0 Å^{-1} to 12.5 Å^{-1} for the pl-Pt electrode kept in the high potential region and for the Sn standard materials (β-Sn foil and SnO$_2$), respectively. The single peak at $R = 1.54$ Å in the RSFs

Fig. 7 κ^3-weighted EXAFS functions ($\kappa^3\chi$ vs. κ curves) obtained from the Sn K-edge XAS spectra for the pl-Pt electrode kept at − 0.05 V, 0.25 V, and 0.65 V (RHE)

Fig. 8 Radial structure functions, RSFs (FT[$\kappa^3\chi(k)$] vs. R curves) obtained by Fourier transforming the EXAFS data in the κ range of 2.0 Å^{-1} to 11.0 Å^{-1} for **a** the pl-Pt electrode kept in the low potential region and for **b** the Sn standard materials (β-Sn and SnO$_2$), respectively
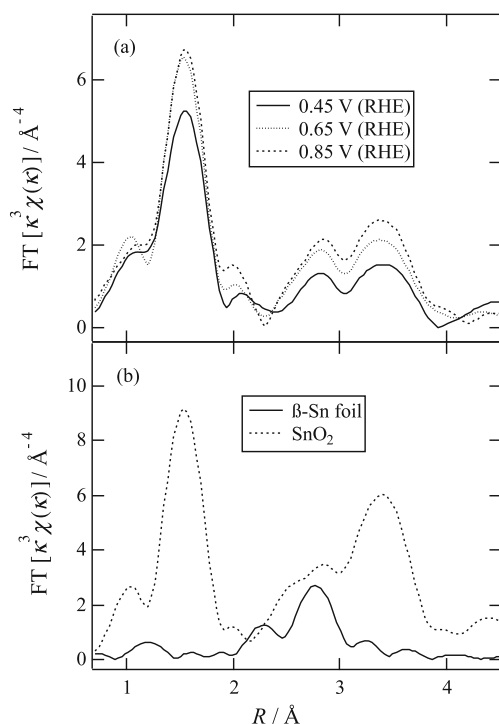
Fig. 9 Radial structure functions, RSFs (FT[$\kappa^3\chi(k)$] vs. R curves) obtained by Fourier transforming the EXAFS data in the κ range of 2.0 Å^{-1} to 12.5 Å^{-1} for **a** the pl-Pt electrode kept in the high potential region and for **b** the Sn standard materials (β-Sn and SnO$_2$), respectively

of the pl-Pt electrode (Fig. 9a) is very close to that $R = 1.53$ Å in the RSF of SnO$_2$ (Fig. 9b). In contrast to Fig. 8a, there is no clear doublet or broad peak at $R = 2.3\sim2.7$ Å in Fig. 9a. However, new doublet peak appears at $R = 2.82\sim3.40$ Å in Fig. 9a, which is close to the multiple peak at $R = 2.85\sim3.41$ Å in the RSF of SnO$_2$ (Fig. 9b). The above comparison suggests that the single peak at $R = 1.54\sim1.63$ Å in Figs. 8a and 9a is associated with the interaction between the nearest neighbor Sn and O atoms (1st shell), while the doublet or broad peak at $R = 2.3\sim2.7$ Å in Fig. 8a is associated with the interactions between the nearest neighbor Sn and Pt or Sn atoms (1st shell). Moreover, the doublet peak at $R = 2.82\sim3.40$ Å in Fig. 9a is associated with the interaction between the nearest neighbor Sn and Sn atoms in oxide (1st shell) or the second near neighbor Sn and O or Sn atoms (2nd shell).

EXAFS parameters of the Sn surface structure on pl-Pt electrode

All peaks in RSF are usually shifted to short distance compared to the real inter-atomic distance due to the phase shift associated with interaction of the photoelectron wave with the potential of the absorbing and the backscattering atoms. For determination of the EXAFS parameters (N, coordination number; d, inter-atomic distance; σ^2, Debye-Waller factor; ΔE_o, energy shift; R_f, R-factor (goodness-of-fit)) for the

Sn-UPD on pl-Pt electrode in the potential range between − 0.05 and 0.25 V (RHE) in Fig. 8a, two different surface structure models of Sn overlayer and Sn incorporation are proposed as shown schematically in Fig. 10. A flat Pt (100) plane is tentatively chosen as the uppermost surface of the pl-Pt electrode exposed to the solution since the Pt leafy structure in Fig. 2 is mainly oriented to the (200) plane. In the Sn overlayer model, Sn atom occupies four-hold hollow site of the nearest neighbor Pt atoms for the Pt (100) plane, while in the Sn-incorporation model, Sn atom is substituted like a surface alloy at face-center-cubic (fcc) site of Pt. In both models, Sn atoms are further bound with O atoms, although the number of O atoms bound with Sn atom and the orientation of the Sn–O bond are arbitrarily chosen in Fig. 10. Furthermore, the Sn–Sn bond is also taken into consideration for both models, although the configuration of the nearest neighbor Sn atoms is not depicted in Fig. 10 to avoid the complexity. The RSF based on the proposed model is simulated and the curve fitting is performed between the simulated and measured RSFs using the program FEFF 8.20 [60, 61]. As a result, the Sn overlayer model gave a good fit as compared to the Sn-incorporation model. Figure 11a, b shows the curve fitting results of the RSFs for the pl-Pt electrode kept at − 0.05 V and 0.15 V (RHE), made on basis of the Sn overlayer model. The EXAFS parameters determined by the curve fitting in the potential
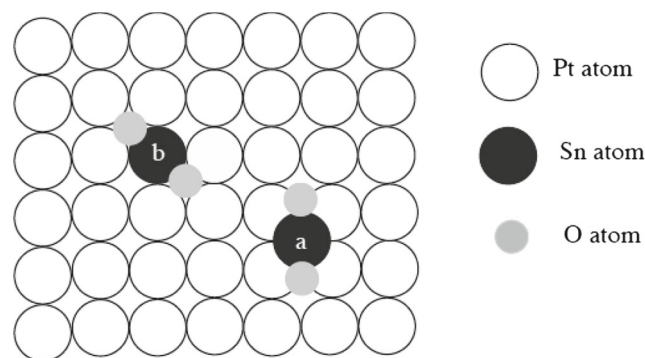
a: Sn-overlayer model
b: Sn-incorporation model

Sn adsorption structure on Pt (100)

Fig. 10 Two different surface structure models of (a) Sn overlayer and (b) Sn incorporation. A flat Pt (100) plane is tentatively chosen as the uppermost surface of the pl-Pt electrode exposed to the solution. In the Sn overlayer model, Sn atom occupies four-hold hollow site of the nearest neighbor Pt atoms for the Pt (100) plane, while in the Sn incorporation model, Sn atom is substituted like a surface alloy at face-center-cubic (fcc) site of Pt. In both models, Sn atoms are further bonded with O atoms, although the number of O atoms bonded with Sn atom and the orientation of Sn–O bond is arbitrarily chosen in Fig. 10. Furthermore, the Sn–Sn bond is also taken into consideration for both models, although the configuration of the nearest neighbor Sn atoms is not depicted in Fig. 10 to avoid the complexity
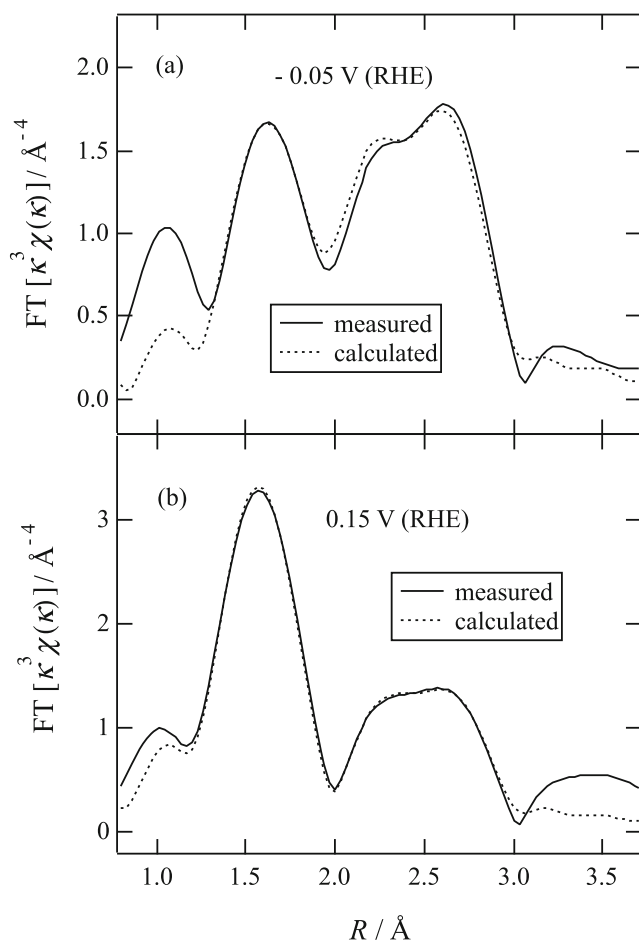
Fig. 11 Fitting results of the RSFs for the pl-Pt electrode kept at **a** − 0.05 V and **b** 0.15 V (RHE), made on the basis of the Sn overlayer model

Table 1 EXAFS parameters determined by curve fitting of the RSFs for the pl-Pt electrode kept in the potential range between − 0.05 and 0.25 V (RHE)

E/V (RHE)		− 0.05	0.05	0.15	0.25
1st shell Sn–O	N	0.88	1.45	2.07	2.57
	d (Å)	2.07	2.03	2.05	2.05
	σ^2 (Å^2)	0.0026	0.0026	0.0026	0.0026
	ΔE_o (eV)	4.19	− 1.76	3.27	3.33
1st shell Sn–Pt	N	3.98	3.70	3.18	2.07
	d (Å)	2.69	2.68	2.70	2.71
	σ^2 (Å^2)	0.0091	0.0091	0.0091	0.0091
	ΔE_o (eV)	0.80	− 1.54	0.64	2.69
1st shell Sn–Sn	N	0.25	0.10	0.09	0.09
	d (Å)	2.69	2.69	2.70	2.72
	σ^2 (Å^2)	0.0091	0.0091	0.0091	0.0091
	ΔE_o (eV)	0.05	− 6.54	6.93	6.83
R_f		0.0042	0.0082	0.0076	0.0037

N, coordination number; d, inter-atomic distance; σ^2, Debye-Waller factor; ΔE_o, energy shift; R_f, R-factor (goodness-of-fit). The simulation was made on basis of the Sn overlayer model

region between − 0.05 and 0.25 V (RHE) are listed in Table 1. The coordination number, N_{Sn-Pt}, of the Sn–Pt bond or, N_{Sn-Sn}, of the Sn–Sn bond decreases with increasing potential, while N_{Sn-O} of the Sn–O bond increases reversely, indicating that the oxidation state of the Sn species on pl-Pt electrode increases with increasing potential. The value of N_{Sn-Pt} at − 0.05 V (RHE) is close to 4, supporting that the pl-Pt electrode is mainly oriented to the (200) plane. Nevertheless, the value of N_{Sn-Sn} at − 0.05 V (RHE) is 0.25, much less than that of N_{Sn-Pt}, which may result from high disorder of the Sn adsorption sites on pl-Pt electrode.

It is remarked that the inter-atomic distance, d_{Sn-Pt}, of the Sn–Pt bond is 2.68~2.71 Å, which is significantly short as compared to that (d_{Sn-Pt} = 2.79 Å) estimated from a hard-sphere model for bulk metals, assuming the atomic radii of bulk Sn (for α-Sn) and Pt being r_{Sn} = 1.405 Å and r_{Pt} = 1.385 Å, respectively. The value of d_{Sn-Sn} = 2.69~2.72 Å is also significantly short as compared to that (d_{Sn-Sn} = 2.81 Å) estimated from the hard-sphere model. Our previous EXAFS analysis [47] of Sn-UPD on surface-roughened (sr-) Ni in 0.2 M HClO$_4$ containing 10^{-3} M Sn^{2+} has also shown that the inter-atomic distance, d_{Sn-Ni}

= 2.55~2.57 Å, of the Sn–Ni bond is significantly short as compared to that (d_{Sn-Ni} = 2.655 Å) estimated from the hard-sphere model for bulk metals, assuming the atomic radii of r_{Sn} = 1.405 Å and r_{Ni} = 1.25 Å. However, the situation seems different between Sn-UPD on sr-Ni and pl-Pt electrodes. In the case of Sn-UPD on sr-Ni electrode, Sn atoms are substituted like a surface alloy at fcc sites in the first Ni layer, i.e., the Sn-incorporation model is operative. The significant reduction in effective radius of the adsorbate at the formation of surface alloy was reported for the Sn monolayer vapor-deposited on Ni (111) [62, 63] or on Cu (111) [64], and for the Pb monolayer vapor-deposited on Ni (111) [65]. On the other hand, the significant reduction in effective radius of the Sn adsorbate at the formation of surface alloy was not reported for the Sn monolayer vapor-deposited on Pt (111) [66] and Pt (100) [67]. The value of d_{Sn-Pt} = 2.78 Å for the surface alloys, $(\sqrt{3} \times \sqrt{3})R30^o$ -Sn/Pt (111) [66] and c(2 × 2) -Sn/Pt (100) [67], is close to that (d_{Sn-Pt} = 2.79 Å) estimated from the hard-sphere model and is slightly less than that (d_{Sn-Pt} = 2.83 Å) [68] for the bulk alloy, Pt$_3$Sn. Therefore, the short inter-atomic distance, d_{Sn-Pt} = 2.68~2.71 Å, for the Sn-UPD on pl-Pt electrode could not be explained in terms of the surface alloy formation.

From another viewpoint, it has been reported that the inter-atomic distance of the Pt–Pt bond [69] or Sn–Pt bond [33] obtained by EXAFS analyses shortens in the case where the average diameter of Pt particles for Pt electrocatalysts (or modified with Sn) is less than a critical size of about 3 nm. The short inter-atomic distance of the Pt–Pt bond for Pt

nanoparticles has been confirmed by TEM observation of Pt aggregates on a thin alumina film [70] and predicted by DFT calculations for small Pt clusters [71]. In the present study, however, the short inter-atomic distance of the Sn–Pt bond (d_{Sn-Pt} = 2.68~2.71 Å) is not consistent with the results of TEM observation of the pl-Pt deposit which show that an average size of Pt particles is significantly larger than 3 nm. In addition, Inoue et al. [35] obtained the similar contradictory results between the inter-atomic distance of Sn–Pt bond (d_{Sn-Pt} = 2.61 ± 0.01 Å) evaluated by EXAFS analysis at Sn K-edge and the average size (4.1 nm) of catalyst particles observed by TEM for bimetallic Pt–Sn/SiO$_2$ catalysts (Sn/Pt = 0.26), which was ascribed to the difference between the actual Debye-Waller factor and the Gaussian approximation used in the EXAFS analysis. However, there were no clear explanations for the contradictory result.

Tentative introduction of cumulant terms for the short inter-atomic distance of the Sn–Pt bond or Sn–Sn bond

Clausen et al. [72] have reported that the anharmonic motion of Pt nanoparticles and the deviation of real Debye-Waller factor from the Gaussian approximation lead to the underestimation of the inter-atomic distance. The most standard approach to analyzing the EXAFS involves quantifying the atom-atom pair distribution extracted from the data by approximating it to the Gaussian distribution [24–26, 73]. However, it has been argued that the atom-atom pair distribution of highly dispersed or disordered systems such as catalytic nanoparticles deviates from the Gaussian pair distribution due to dynamic (thermal) or static (structural) disorder [74–77]. Furthermore, it has been shown that the atom-atom pair distribution deviates from the Gaussian in disordered solids such as β-AgI [78]. In the case where the atom-atom pair distribution is not Gaussian, i.e., asymmetric, it has been pointed out that the standard EXAFS analysis based on the assumption of the Gaussian pair distribution leads to the underestimation of inter-atomic distance and coordination number. The introduction of cumulant terms, C_3 and C_4, in the standard EXAFS formula has been employed as a measure of the deviation of the pair distribution function from the Gaussian shape [74–77]. The standard EXAFS formula in the single scattering approximation for the first shell can be written as:

$$\chi(\kappa) = A(\kappa)\sin[\psi(\kappa)], \tag{2}$$

where the amplitude, $A(\kappa)$, and the phase of the EXAFS, $\psi(\kappa)$, are given by

$$A(\kappa) = \frac{N}{\kappa d^2} F(\kappa) exp\left(-\frac{2d}{\lambda(\kappa)}\right) exp\left(-2\kappa^2\sigma^2\right), \tag{3}$$

and

$$\psi(\kappa) = 2\kappa d + \delta(\kappa), \tag{4}$$

where N is the coordination number, $F(\kappa)$ is the backscattering amplitude, d is the mean inter-atomic distance, $\lambda(\kappa)$ is the electron mean-free path, σ^2 is the Debye-Waller factor, and $\delta(\kappa)$ is the phase shift. For the cumulant expansion approach [75, 76], the terms of C_3 and C_4 or higher-order cumulants are added to Eqs. (3) and (4), i.e.,

$$A(\kappa) = \frac{N}{\kappa d^2} F(\kappa) exp\left(-\frac{2d}{\lambda(\kappa)}\right) exp\left(-2\kappa^2\sigma^2 + \frac{2}{3}C_4\kappa^4\cdots\right), \tag{5}$$

and

$$\psi(\kappa) = 2\kappa d + \delta(\kappa) - \frac{4}{3}C_3\kappa^3 + \cdots. \tag{6}$$

The short inter-atomic distance of the Sn–Pt bond or Sn–Sn bond obtained by the standard EXAFS analysis in the present study may result from the non-Gaussian distribution of the Sn adsorption sites on the pl-Pt electrode although the distribution of the Sn adsorption sites on the pl-Pt electrode has not been reported so far. It would be worthy to examine how to change the inter-atomic distance and coordination number of the Sn–Pt bond or Sn–Sn bond by introducing the cumulant terms of C_3 and C_4 in EXAFS analysis. Accordingly, the EXAFS analysis including the cumulant terms of C_3 (in the order of 10^{-4} Å^3) and C_4 (in the order of 10^{-5} Å^4) was tentatively made in the κ window of 2.0 to 11 Å^{-1} for the Sn–Pt bond or Sn–Sn bond to obtain the best fits with real EXAFS data. The best fits were obtained in the potential range between − 0.05 and 0.25 V (RHE) when the values of C_3 = 7.27 × 10^{-4} Å^3 and C_4 = − 5.0 × 10^{-5} Å^4 were chosen by try and errors. Figure 12a, b shows the fitting results of the RSFs involving the C_3 and C_4 terms for the pl-Pt electrode at − 0.05 V and 0.15 V (RHE), respectively. The EXAFS parameters determined with the fitting results of the RSFs involving the C_3 and C_4 terms for the pl-Pt electrode in the potential range between − 0.05 and 0.25 V (RHE) are listed in Table 2.

The comparison between Tables 1 and 2 indicates that the cumulant term of C_3 = 7.27 × 10^{-4} Å^3 stretches both d_{Sn-Pt} and d_{Sn-Sn} by 0.06~0.09 Å so as to approach closely to that (2.78 Å) speculated from the particle size of the pl-Pt deposit, while the cumulant term of C_4 = − 5.0 × 10^{-5} Å^4 lowers the value of N_{Sn-Pt} by 0.43~0.07 and the value of N_{Sn-Sn} by 0.72~0.36, depending on potential. The lowering of N_{Sn-Pt} and N_{Sn-Sn} results from the minus value of C_4 which also contributes to the lowering of the Debye-Waller factor for the Sn–Pt and Sn–Sn bonds. The values of N_{Sn-Pt} = 3.98 at − 0.05 V (RHE) and of N_{Sn-Pt} = 3.70 at 0.05 V (RHE) in Table 1 may be rather overestimated if the participation in the (111) orientation of the pl-Pt electrode is taken into consideration for the Sn overlayer model. The involvement of C_3 = 7.27 × 10^{-4} Å^3
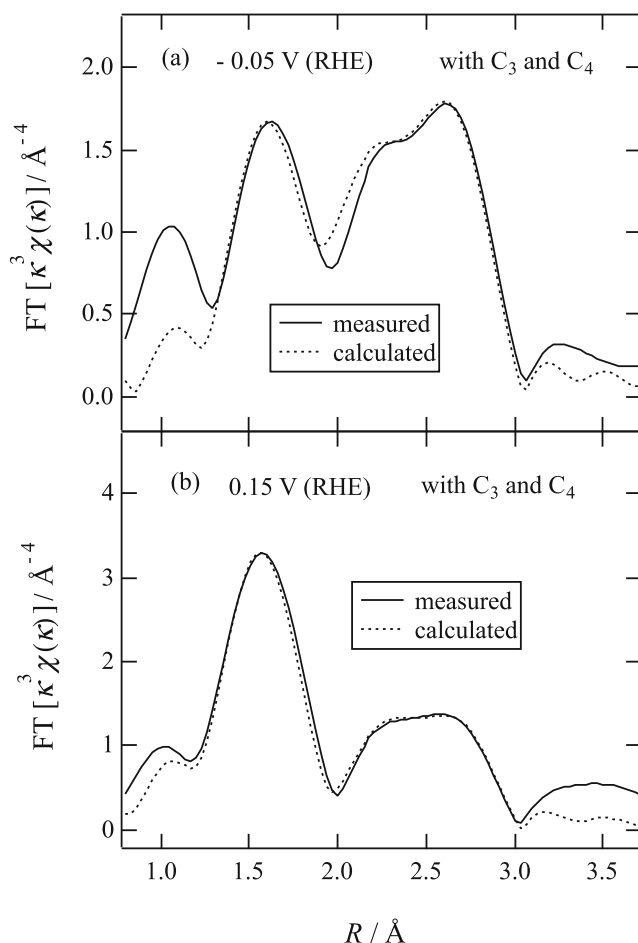
Fig. 12 Fitting results of the RSFs involving the C_3 and C_4 terms for the pl-Pt electrode kept at **a** -0.05 V and **b** 0.15 V (RHE). The cumulant terms of $C_3 = 7.27 \times 10^{-4}$ Å^3 and $C_4 = -5.0 \times 10^{-5}$ Å^4 were chosen for the fitting

Table 2 EXAFS parameters determined by curve fitting of the RSFs involving the third and fourth cumulants for the pl-Pt electrode kept in the potential range between -0.05 and 0.25 V (RHE)

E/V (RHE)		-0.05	0.05	0.15	0.25
1st shell Sn–O	N	0.93	1.43	2.05	2.55
	d (Å)	2.08	2.05	2.06	2.05
	σ^2 (Å^2)	0.0026	0.0026	0.0026	0.0026
	ΔE_o (eV)	4.57	4.67	5.04	6.83
1st shell Sn–Pt*	N	3.55	3.45	2.97	2.00
	d (Å)	2.77	2.77	2.77	2.77
	σ^2 (Å^2)	0.0080	0.0080	0.0080	0.0080
	ΔE_o (eV)	6.21	6.02	5.82	2.69
1st shell Sn–Sn*	N	0.97	0.66	0.50	0.45
	d (Å)	2.77	2.78	2.77	2.78
	σ^2 (Å^2)	0.0080	0.0080	0.0080	0.0080
	ΔE_o (eV)	4.57	4.67	5.04	6.83
R_f		0.023	0.018	0.0073	0.011

N, coordination number; d, inter-atomic distance; σ^2, Debye-Waller factor; ΔE_o, energy shift; R_f, R-factor (goodness-of-fit). The simulation was made on basis of the Sn overlayer model

*The cumulant terms of $C_3 = 7.28 \times 10^{-4}$ Å^3 and $C_4 = -5.0 \times 10^{-5}$ Å^4 were used for the 1st shells of Sn–Pt and Sn–Sn interactions

and $C_4 = -5.0 \times 10^{-5}$ Å^4 does not influence significantly the value of $N_{\text{Sn-O}}$ and its potential dependence, but it improves the fluctuation in potential dependence of $d_{\text{Sn-O}}$ since the value of $d_{\text{Sn-O}}$ in Table 2 as compared to that in Table 1 decreases smoothly from 2.08 to 2.05 Å with increasing potential in the potential range between -0.05 and 0.25 V (RHE). However, there have been no clear evidences that the atom-atom pair distribution of the Sn adsorption sites on the pl-Pt electrode deviates from the Gaussian. As shown in Fig. 1a, the pl-Pt electrode has a columnar structure like a cauliflower. The atom-atom pair distribution of the Sn adsorption sites may vary in depth direction of the pl-Pt electrode to bring forth the deviation from the Gaussian.

Difference in Sn species on Pt between the present and previous results

Although unsolved issue remains for the deviation from the Gaussian, it is emphasized that the presence of the Sn–Pt and Sn–Sn bonds in addition of the Sn–O bond is confirmed for

the first time in the potential region of Sn-UPD on Pt. It is remarked that the EXAFS results [31] made by Mukerjee and McBreen at Sn K-edge of the Sn-UPD on carbon-supported Pt electrocatalyst in 0.5 M H$_2$SO$_4$ are not consistent with the present results in Table 1 or Table 2 since any Sn–Pt and Sn–Sn bonds except for Sn–O bond are not found. The XAS experiments [31] were carried out in 0.5 M H$_2$SO$_4$ free from Sn^{4+} after the Sn-UPD on carbon-supported Pt under potentiostatic polarization at 0.33 V (RHE) for 3.75 h in 0.5 M H$_2$SO$_4$ containing 3×10^{-3} M SnCl$_4$. Consequently, the Sn K-edge EXAFS parameters obtained by Mukerjee and McBreen [31] are restricted to the Sn species irreversibly adsorbed and remained on Pt in 0.5 M H$_2$SO$_4$. In contrast, the Sn K-edge EXAFS parameters (Tables 1 or 2) obtained by the present study are responsible for the total Sn species adsorbed on pl-Pt electrode in 0.2 M HClO$_4$ containing 10^{-3} M Sn^{2+}. The oxidation state of the Sn species irreversibly adsorbed and remained on Pt in 0.5 M H$_2$SO$_4$ may be different from that of the total Sn species adsorbed on Pt in equilibrium with Sn^{2+} in solution. Furthermore, it is not excluded that the Sn species adsorbed on the carbon-supported Pt is likely oxidized during the exchange to the solution free from Sn^{4+}. In many cases of Pt electrocatalysts modified with Sn, Sn is incorporated into Pt lattice to form a bimetallic phase such as Pt–Sn alloy [2–4, 14–18, 79]. On the other hand, the present study has indicated that the Sn-UPD layer on pl-Pt electrode in solution containing Sn^{2+} is not incorporated into Pt lattice and thus a bimetallic phase is not formed.

In the potential region between 0.45 and 0.85 V (RHE), no metallic bonds of Sn–Pt and Sn–Sn are observed. For determination of the EXAFS parameters for the Sn species on pl-Pt electrode in the potential range between 0.45 and 0.85 V (RHE) in Fig. 9a, the RSFs were calculated by assuming that the Sn species is oxidized to form a surface oxide. Figure 13a, b shows the curve fitting results of the RSFs for the pl-Pt electrode at 0.45 V and 0.65 V (RHE), respectively. The EXAFS parameters determined with the curve fitting of the RSFs for the pl-Pt electrode in the potential range between 0.45 and 0.85 V (RHE) are listed in Table 3. As shown in Table 3, d_{Sn-O} at the first shell is nearly equal to that of the standard SnO_2 (cassiterite), while N_{Sn-O} and N_{Sn-Sn} at the first and second shells increase with increasing potential, reflecting on the increase in oxidation state of the Sn species adsorbed on the pl-Pt electrode. However, the values of N_{Sn-O} and N_{Sn-Sn} are less than the corresponding values of the standard SnO_2 suggesting that the Sn surface oxide is different from the bulk oxide with three dimensions. Nakamura et al. [79] have reported that the Sn species irreversibly adsorbed on Pt (111) is not anodically dissolved in 0.1 M $HClO_4$ to remain as an oxidation state on the surface. The XANES and EXAFS data of Sn
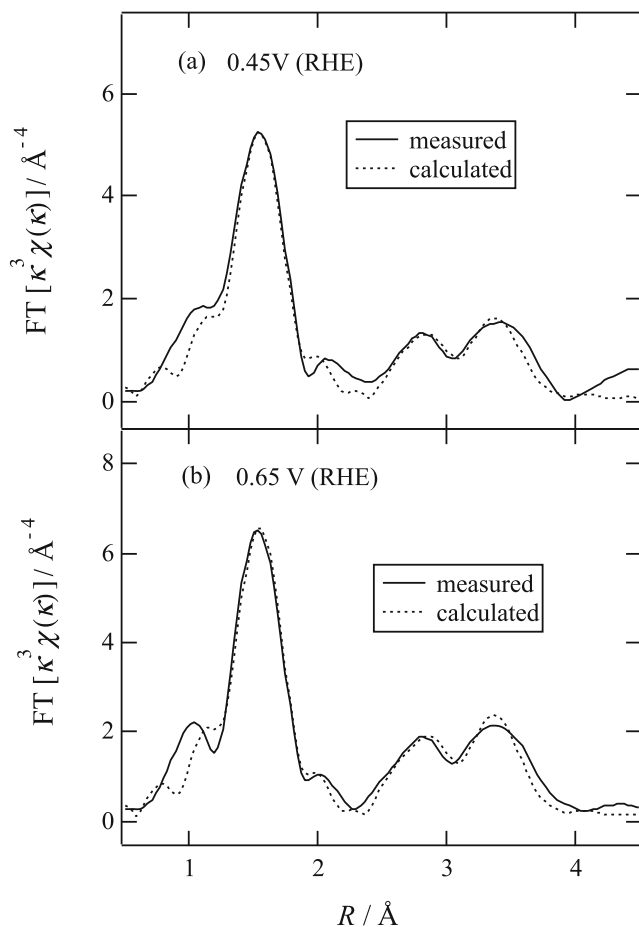
Table 3 EXAFS parameters determined with curve fitting of the RSFs for the pl-Pt electrode kept in the potential range between 0.45 and 0.85 V (RHE), and for the standard SnO_2 powder

E/V (RHE)		0.45	0.65	0.85	SnO_2
1st shell Sn–O	N	3.60	4.50	4.55	6.00
	d (Å)	2.05	2.05	2.05	2.05
	σ^2 (Å²)	0.0031	0.0031	0.0031	0.031
	ΔE_o (eV)	2.75	2.46	2.54	3.89
1st shell Sn–Sn	N	0.58	0.94	1.15	2.00
	d(Å)	3.15	3.16	3.18	3.19
	σ^2 (Å²)	0.0030	0.0030	0.0030	0.030
	ΔE_o(eV)	2.75	2.46	2.54	3.89
2nd shell Sn–O	N	2.73	3.30	3.33	4.00
	d(Å)	3.46	3.49	3.54	3.58
	σ^2 (Å²)	0.0070	0.0070	0.0070	0.0070
	ΔE_o (eV)	2.75	2.46	2.54	3.89
2nd shell Sn–Sn	N	2.17	3.00	3.56	8.00
	d (Å)	3.73	3.73	3.72	3.71
	σ^2 (Å²)	0.0060	0.0060	0.0060	0.0060
	ΔE_o (eV)	2.75	2.46	2.54	3.89
R_f		0.022	0.015	0.013	0.037

N, coordination number; d, inter-atomic distance; σ^2, Debye-Waller factor; ΔE_o, energy shift; R_f, R-factor (goodness-of-fit). The simulation was made by assuming that the Sn species is oxidized to form a surface oxide

K-edge by Mukerjee and McBreen [31] have suggested that the oxidation state of the Sn species remained on carbon-supported Pt in 0.5 M H_2SO_4 is divalent in the potential range between 0.0 and 0.54 V (RHE). The oxidation state of the Sn species on Pt in the present results is quite different from that in the previous results [31] since the XAS measurements of the Sn species on the pl-Pt electrode in the present study are performed in 0.2 M $HClO_4$ containing 10^{-3} M Sn^{2+}. According to the potential-pH equilibrium diagram of the Sn/H_2O system [80], SnO_2 or $Sn(OH)_4$ is thermodynamically stable in 0.2 M $HClO_4$ containing 10^{-3} M Sn^{2+} at the potentials more positive than about 0.1 V (RHE). In the present study, it is suggested that Sn^{2+} in 0.2 M $HClO_4$ is partly oxidized to Sn^{4+} in the potential range between 0.45 and 0.85 V (RHE) to precipitate as SnO_2 or $Sn(OH)_4$ on the pl-Pt electrode, which supports the results of Table 3.

Conclusions

In situ XAS combined with the periodical emersion method was employed to investigate the Sn species adsorbed on the pl-Pt electrode in 0.2 M $HClO_4$ solution containing 10^{-3} M Sn^{2+}. The Sn K-edge adsorption spectra in a scanning XAS mode measured by monitoring the Sn $K_{\alpha 1}$ fluorescence line has indicated that a large roughness factor of $S_r = 770$ for the

Fig. 13 Fitting results of the RSFs for the pl-Pt electrode kept at **a** 0.45 V and **b** 0.65 V (RHE). The RSFs were calculated by assuming that the Sn species is oxidized to form a surface oxide

pl-Pt electrode is sufficient to detect sensitively the sub-monolayer coverage of Sn on Pt. The XANES has revealed that the Sn species adsorbed on the pl-Pt electrode is partly oxygenated in the potential region between − 0.05 and 0.25 V (RHE) where the Sn-UPD is overlapped with the UPD of hydrogen on Pt. The EXAFS analysis has supported a Sn overlayer model in which Sn atom occupies the hollow site of the nearest neighbor Pt atoms and is further bonded with oxygen atom in the Sn-UPD region. The coordination number of the Sn–Pt bond, N_{Sn-Pt}, or Sn–Sn bond, N_{Sn-Pt}, decreases with increasing potential, while the coordination number of the Sn–O bond increases reversely.

The essential issue for the EXAFS analysis in the present study is that the inter-atomic distance of the Sn–Pt bond, d_{Sn-Pt} = 2.68~2.71 Å, is significantly short as compared to that (d_{Sn-Pt} = 2.79 Å) estimated from a hard-sphere model for bulk metals, assuming that the atomic radii of bulk Sn (for α-Sn) and Pt are r_{Sn} = 1.405 Å and r_{Pt} = 1.385 Å, respectively. The short inter-atomic distance of the Sn–Pt bond is also inconsistent with that predicted from the average particle size and lattice image of the pl-Pt deposit observed by TEM with an atomic resolution. The deviation from the Gaussian for atom-atom pair distribution of the Sn adsorption sites on the pl-Pt electrode may be the main cause for the short inter-atomic distance. The cumulant terms, C_3 and C_4, are tentatively introduced to correct the deviation from the Gaussian distribution.

The best fit with the measured EXAFS results was achieved by introducing the values of $C_3 = 7.27 \times 10^{-4}$ Å^3 and $C_4 = - 5.0 \times 10^{-5}$ Å^4 for the first shells of the Sn–Pt and Sn–Sn interactions. The cumulant term of $C_3 = 7.27 \times 10^{-4}$ Å^3 stretches both d_{Sn-Pt} and d_{Sn-Sn} by 0.06~0.09 Å so as to approach closely to that (2.78 Å) speculated from the average particle size of the pl-Pt deposit, while the cumulant term of $C_4 = - 5.0 \times 10^{-5}$ Å^4 lowers not only the Debye-Waller factors for the Sn–Pt and Sn–Sn bonds but also lowers N_{Sn-Pt} by 0.43~0.07 and N_{Sn-Sn} by 0.72~0.36, respectively, depending on potential.

However, there have been no clear evidences that the atom-atom pair distribution of the Sn adsorption sites on the pl-Pt electrode deviates from the Gaussian. The atom-atom pair distribution of the Sn adsorption sites may vary in depth direction of the pl-Pt electrode with a columnar structure like a cauliflower, which would bring forth the deviation from the Gaussian. Despite the unsolved issue for the deviation from the Gaussian, it is confirmed for the first time that the Sn species adsorbed on Pt in equilibrium with Sn^{2+} in solution is partly bounded with Pt and Sn atoms in addition to oxygen atom in the Sn-UPD potential region between − 0.05 and 0.25 V (RHE). By contrast, in the potential region between 0.45 and 0.85 V (RHE) where no metallic bonds of the Sn–Pt and Sn–Sn are observed, it is suggested that two-dimensional surface Sn oxide or hydroxide forms, which is supported from the potential-pH equilibrium diagram of the Sn/H$_2$O system.

References

1. Motoo S, Shibata M, Watanabe M (1980) J Electroanal Chem 110(1-3):103–109
2. Gasteiger HA, Markovic NM, Ross PN (1995) J Phys Chem 99(22):8945–8949
3. Antolini E, Gonzalez ER (2010) Electrochim Acta 56(1):1–14
4. Stevanović S, Tripković D, Tripković V, Minić D, Gavrilović A, Tripkvíc A, Jovanovíc VM (2014) J Phys Chem C 118(1):278–289
5. Motoo S, Watanabe M (1976) J Electroanal Chem 69(3):429–413
6. Watanabe M, Furuuchi Y, Motoo S (1985) J Electroanal Chem 191(2):367–375
7. Vassiliev YB, Bagotzky VS, Osetrova NV, Mikkailova AA (1979) J Electroanal Chem 97(1):63–76
8. Sobkowski J, Franaszczuk K, Piasecki A (1985) J Electroanal Chem 196(1):145–156
9. Wei ZD, Li LL, Luo YH, Yan C, Sun CX, Yin GZ, Shen PK (2006) J Phys Chem B 110(51):26055–26061
10. Beden B, Kadirgan F, Lamy C, Leger JM (1981) J Electroanal Chem 127(1-3):75–85
11. Haner AN, Ross PN (1991) J Phys Chem 95(9):3740–3746
12. Campbell SA, Parson R (1992) J Chem Soc Faraday Trans 88(6): 833–841
13. Lamy-Pitara E, Quazzani-Benhima EE, Barbier J, Cahoreau M, Caisso J (1994) J Electroanal Chem 372(1-2):233–242
14. Janssen MMP, Moolhuysen J (1976) Electrochim Acta 21(11):861–868
15. Janssen MMP, Moolhuysen J (1977) J Catal 46(3):289–296
16. Wang K, Gasteiger HA, Markovic NM, Ross PN (1996) Electrochim Acta 41(16):2587–2593
17. Stamenkovic V, Aren M, Blizanac BB, Mayrhofer KJJ, Ross PN, Markovic NM (2005) Surf Sci 576(1-3):145–157
18. Liu Z, Reed D, Kwon G, Shamsuzzoha M, Nikles DE (2007) J Phys Chem C 111(38):14223–14229
19. Cathro KJ (1969) J Electrochem Soc 116(11):1608–1611
20. Katayama A (1980) J Phys Chem 84(4):376–381
21. Schryer DR, Upchurch BT, Van Norman JD, Brown KG, Schryer J (1990) J Catal 122(1):193–197
22. Aramata A, Toyoshima I, Enyo M (1992) Electrochim Acta 37(8): 1317–1320
23. Grass K, Lintz H-G (1997) J Catal 172(2):446–452
24. Abruna HD (1991) In: Abruna HD (ed), Modern techniques for in-situ interface charctrerization Electrochemical interfaces chapt 1. Modern techniques for in-situ interface charctrerization. VCH Pub Inc, New York
25. Bunker G (2010) Introduction to XAFS. A practical guide to X-ray absorption fine structure spectroscopy. Cambridge University Press, Cambridge
26. Nagy Z (2011) J Solid State Electrochem 15(7-8):1679–1695
27. Russell AE, Rose A (2004) Chem Rev 104(10):4613–4635
28. Meitzner G, Via GH, Lytle FW, Fung SC, Sinfelt JH (1988) J Phys Chem 92(10):2925–2932
29. Borgna A, Stagg SM, Resasco DE (1998) J Phys Chem B 102(26): 5077–5081
30. Pinxt HHCM, Kuster BFM, Koningsberger DC, Martin GB (1998) Catal Today 39(4):351–361
31. Mukerjee S, McBreen J (1999) J Electrochem Soc 146(2):600–606
32. Roman-Martinez MC, Cazorla-Amoros D, Yamashita H, de Miguel S, Scelza OA (2000) Langmuir 16(3):1123–1131

33. Ramallo-Lopez JM, Santori GF, Giovanetti L, Casella ML, Ferretti OA, Requejo FG (2003) J Phys Chem B 107(41):11441–11451

34. Melke J, Schoekel A, Dixon D, Cremers C, Ramaker DE, Roth C (2010) J Phys Chem C 114(13):5914–5925

35. Inoue T, Tomishige K, Iwasawa Y (1996) J Chem Soc Faraday Trans 92(3):461–467

36. Hansen WN, Wang CL, Humpherys TW (1978) J Electroanal Chem 93(2):87–98

37. Kolb DM, Hansen WN (1979) Surf Sci 79(1):205–211

38. Stefan IC, Scherson DA (2003) J Electroanal Chem 554-555:361–366

39. Samant MG, Borges GL, Gordon JG II, Melroy OR, Blum L (1987) J Am Chem Soc 109(20):5970–5974

40. Melroy OR, Samant MG, Borges GL, Gordon JG II, Blum L, White JH, Albarelli MJ, MicMillan M, Abruna HD (1988) Langmuir 4(3):728–732

41. Tadjeddine A, Tourillon G, Guay D (1991) Electrochim Acta 36(11-12):1859–1862

42. Tadjeddine A, Lahrichi A, Tourillon G (1993) J Electroanal Chem 360(1-2):261–270

43. Soldo Y, Sibert E, Tourillon G, Hazemann JL, Lévy JP, Aberdam D, Faure R, Durand R (2002) Electrochim Acta 47(19):3081–3091

44. Durand R, Faure R, Aberdam D, Salem C, Tourillon G, Guay D, Ladouceur M (1992) Electrochim Acta 37(11):1977–1982

45. Lee JRI, O'Malley RL, O'Connell TJ, Vollmer A, Rayment T (2010) Electrochim Acta 55(28):8532–8538

46. Seo M, Fushimi K, Aoki Y, Habazaki H, Inaba M, Yokomizo M, Hayakawa T, Nakayama T (2012) J Electroanal Chem 671:7–15

47. Seo M, Habazaki H, Inaba M, Yokomizo M, Wakabayashi T, Nakayama T (2014) J Electrochem Soc 161(4):H195–H202

48. Feltham AM, Spiro M (1971) Chem Rev 71(2):177–193

49. Seo M, Hyono A, Habazaki H, Nakayama T (2014) J Electrochem Soc 161(12):C550–C556

50. Du K, Ernst F, Pelsozy MC, Barthel J, Tillmann K (2010) Acta Mater 58(3):836–845

51. Gilman S (1964) Electrochim Acta 9(7):1025–1046

52. Brummer SB (1965) J Phys Chem 69(2):562–571

53. Brummer SB, Ford JI, Turner MJ (1965) J Phys Chem 69(10):3424–3433

54. Woods R (1968) Electrochim Acta 13(10):1967–1972

55. Biegler T (1969) J Electrochem Soc 116(8):1131–1137

56. Kolb DM, Przasnyski M, Gerischer H (1974) J Electroanal Chem 54(1):25–38

57. Kolb DM (1978) In: Gerischer H, Tobias CW (eds) Advances in electrochemistry and electrochemical engineering vol. Wiley, New York, p 1

58. Koma A, Yagi K, Tsukada AM (1987) Handbook of surface physics technology. Maruzen, Tokyo

59. Herrero E, Buller LJ, Abruna HD (2001) Chem Rev 101(7):1897–1930

60. Ankudinov AL, Ravel B, Rehr JJ, Condrason SD (1998) Phys Rev B 58(12):7565–7576

61. Ankudinov AL, Bouldin CE, Rehr JJ, Sim J, Hung H (2002) Phys Rev B 61:104107–104117

62. Ku Y, Overbury SH (1992) Surf Sci 373:341–352

63. Woodruff DP, Vlieg E (2002) In: Woodruff DP (ed) The chemical physics of solid surfaces vol 10. Surface alloys and alloy surfaces, chapt 8. Elsevier Science, Amsterdam

64. Overbury SH, Ku Y (1992) Phys Rev B 46(12):7868–7872

65. Brown D, Quinn PD, Woodruff DP, Bailey P, Noakes CQ (2000) Phys Rev B 61(11):7706–7715

66. Overbury SH, Mullins DR, Paffett MT, Koel BE (1991) Surf Sci 254(1-3):45–57

67. Li YD, Koel BE (1995) Surf Sci 330(2):193–206

68. Woodruff DP, Robinson J (2003) Appl Surf Sci 219(1-2):1–10

69. Yoshitake H, Yamazaki O, Ota K (1994) J Electrochem Soc 141(9):2516–2521

70. Klimenkov M, Nepijko S, Kuhlenbeck H, Bäumer M, Schlögl R, Freund H-L (1997) Surf Sci 391(1-3):27–36

71. Ankudinov AL, Rehr JJ, Low JJ, Bare SR (2002) J Chem Phys 116(5):1911–1919

72. Clausen BS, Grabek L, Topse H, Hansen LB, Stoltze P, Norskov JK, Nielsen OH (1993) J Catal 141(2):368–379

73. Koningsberger DC, Mojet BL, Van Dorssen GE, Ramaker DE (2003) Top Catal 10:143–155

74. Monti F (1996) J Synchrotron Radiat 3(3):129–195

75. Clausen BS, Norskov JK (2000) Top Catal 10(3/4):221–230

76. Bus E, Miller JT, Kropf AJ, Prins R, van Bokhoven JA (2006) Phys Chem Chem Phys 8(27):3248–32358

77. Sanson A (2009) J Synchrotron Radiat 16(6):864–868

78. Dalba G, Fornasini P, Rocca F (1993) Phys Rev B 47:8501–8514

79. Nakamura M, Imai R, Otsuka N, Hoshi N, Sakata O (2013) J Phys Chem C 117(35):18139–18143

80. Pourbaix M (1979) Atlas of electrochemical equilibria in aqueous solutions. NACE, Houston, pp 475–484